(17) C. C. J. Roothaan, *Rev. Mod. Phys.*, **32**, 179–185 (1960).
(18) B. Huron, J. P. Malrieu, and P. Rancurel, *J. Chem. Phys.*, **58**, 5745–5759 (1973).
(19) C. Möller and M. S. Plesset, *Phys. Rev.*, **46**, 618–622 (1934).
(20) E. B. Wilson, J. C. Decius, and P. C. Cross, "Molecular Vibrations", McGraw-Hill, New York, 1955.
(21) G. R. Smith and W. A. Guillory, *J. Chem. Phys.*, **56**, 1423–1430 (1972).
(22) C. Teichteil, J. P. Malrieu, and J. C. Barthelat, *Mol. Phys.*, **33**, 181–197 (1977); R. Ditchfield and K. Seidman, *Chem. Phys. Lett.*, **54**, 57–60 (1978).
(23) H. Takeo, R. F. Curl, and P. W. Wilson, *J. Mol. Spectrosc.*, **38**, 464–475 (1971).
(24) J. W. Hastie, R. Hauge, and J. L. Margrave, *J. Phys. Chem.*, **72**, 4492–4496 (1968).
(25) R. Hauge, V. M. Khanna, and J. L. Margrave, *J. Mol. Spectrosc.*, **27**, 143–147 (1968).
(26) J. W. Hastie, R. H. Hauge, and J. L. Margrave, *J. Mol. Spectrosc.*, **29**, 152–162 (1969).
(27) H. Huber, E. P. Kündig, G. A. Ozin, and A. Vandervoet, *Can. J. Chem.*, **52**, 95–99 (1974).
(28) R. W. Martin and A. J. Merer, *Can. J. Phys.*, **51**, 727–730 (1972).
(29) K. C. Mishra, B. Padhy, and B. S. Mohanty, *Indian J. Pure Appl. Phys.*, **15**, 405–408 (1977).
(30) T. C. Ehlert and J. L. Margrave, *J. Chem. Phys.*, **41**, 1066 (1964).
(31) K. F. Zmbov, J. W. Hastie, J. Hauge, and J. L. Margrave, *Inorg. Chem.*, **7**, 608–609 (1968).
(32) J. L. Margrave and D. L. Perry, *Inorg. Chem.*, **16**, 1820–1822 (1977).
(33) J. Satgé, P. Rivière, and A. Boy, *C. R. Acad. Sci., Ser. C*, **278**, 1309–1312 (1974); P. Rivière, J. Satgé, and A. Boy, *J. Organomet. Chem.*, **96**, 25–40 (1975).
(34) P. Rivière, J. Satgé, and A. Castel, *C. R. Acad. Sci., Ser. C*, **281**, 835–838 (1975).
(35) P. Rivière, J. Satgé, and A. Castel, *C. R. Acad. Sci., Ser. C*, **282**, 971–974 (1976).

Spectroscopic Studies of Photochemically Important Transition Metal Excited States. 2. The $^1T_{1g}$, $^3T_{1g}$, and $^5T_{2g}$ Excited States of Hexaamminecobalt(III)

Randall B. Wilson and Edward I. Solomon*

Contribution from the Department of Chemistry, Massachusetts Institute of Technology, Cambridge, Massachusetts 02139. *Received August 31, 1979*

Abstract: Low-temperature, high-resolution, polarized single crystal absorption studies of the $^1T_{1g} \rightarrow {}^1A_{1g}$, $^3T_{1g} \rightarrow {}^1A_{1g}$ electronic transitions in hexaamminecobalt(III) are reported. Analysis of the structure in the electronic origin regions of these transitions combined with Franck-Condon analysis of the absorption band shapes demonstrates that the photochemically active $^3T_{1g}$ state (and $^1T_{1g}$ state) undergoes a large e_g Jahn-Teller effect. This produces a D_{4h} excited state geometry with an expansion of ~0.12 Å in the Co-NH_3 bond length along two axes and a contraction of ~0.02 Å along the third axis. In addition, an analysis of the multiplet splitting pattern of the $^3T_{1g}$ pure electronic origins allows an approximate determination of the energetic position of the $^5T_{2g}$ state which interacts with the triplet through spin-orbit coupling. An experimentally derived potential surface diagram of the above states is presented which indicates an efficient radiationless deactivation pathway for the $^3T_{1g}$ state. The photochemical implications of these results and their relation to other photochemically active d^3 and d^6 complexes are also discussed.

I. Introduction

In a previous study[1] we were able to experimentally determine a reasonable picture of the equilibrium geometry of the photoactive $^4T_2$ excited state of the d^3 octahedral hexaamminechromium(III) complex. These results were made possible through detailed spectroscopic study of a new molecular crystal lattice system, $Cr(NH_3)_6(ClO_4)_2Cl{\cdot}KCl$, which exhibits a great deal of vibronic structure on the broad band ligand field $^4T_{2g} \leftarrow {}^4A_{2g}$ transition at low temperature. From a theoretical analysis of the origin region and of the overall band shape, it was found that the $Cr(NH_3)_6^{3+}$ complex undergoes reasonably large distortions in both the totally symmetric a_{1g} and Jahn-Teller e_g normal modes upon excitation into the $^4T_{2g}$ excited state. These distortions combine to produce an excited-state molecule with D_{4h} symmetry which is expanded in the equatorial plane, a distortion which is consistent with the observed ligand photodissociation product in the substituted complexes.

In the low-spin d^6 octahedral complexes, particularly $Co(NH_3)_6^{3+}$ and $Co(CN)_6^{3-}$, photochemical studies[2] have implicated the spin-forbidden $^3T_{1g}$ excited state as being responsible for the observed photoreactivity. However, more recent investigations[3] suggest that in $Co(NH_3)_6^{3+}$ the $^3T_{2g}$ and $^1T_{1g}$ states may also play a significant role. These transitions are indicated in the overall $Co(NH_3)_6^{3+}$ absorption spectrum presented in Figure 1.

One particularly striking difference between these two complexes is in their photoaquation quantum yields ($\phi(Co(NH_3)_6^{3+}) = 3.1 \times 10^{-4}$; $\phi(Co(CN)_6^{3-}) = 0.31$).[4a] Possible rationales for these differences involve significant variations[4a,b] in the potential surfaces of the $^3T_{1g}$ state in the hexaammine as compared to the hexacyanide and the effects[4c,d] of the strongly D_q dependent, highly spin forbidden $^5T_{2g}$ state on the $^3T_{1g}$ state in the hexaammine, which has a lower ligand field strength and therefore a lower lying quintet. Although it was possible to determine[5] an average excited state distortion for $Co(CN)_6^{3-}$ by simultaneously fitting the weakly structured emission spectrum and the unstructured absorption spectrum, not enough structure is exhibited by this complex to experimentally distinguish between the different distorting modes and obtain an excited-state geometry. This is in contrast to $Co(NH_3)_6^{3+}$, which does not appear to emit, but which we find to exhibit in its absorption spectrum (like its chromium counterpart) a great deal of excited-state structure in the $Co(NH_3)_3(ClO_4)_2Cl{\cdot}KCl$ lattice. This has permitted us to obtain reasonable pictures of the $^1T_{1g}$ and $^3T_{1g}$ excited state geometries. Furthermore, the highly structured $^3T_{1g}$ electronic origin region permits us to obtain experimental evidence for a strong $^3T_{1g}$-$^5T_{2g}$ interaction via spin-orbit coupling for this complex and to derive an approximate picture of the potential surfaces and energetic position of the $^5T_{2g}$ state with respect to the $^3T_{1g}$ state. The photochemical implications of these results are considered in the Discussion section.

0002-7863/80/1502-4085$01.00/0

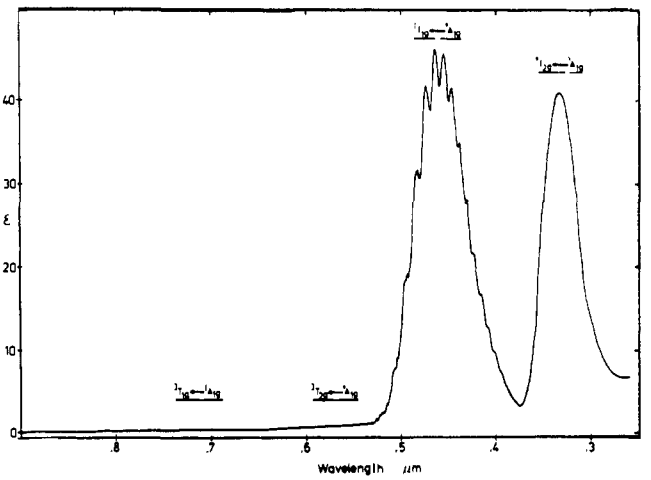

Figure 1. Unpolarized single crystal absorption spectrum of $Co(NH_3)_6(ClO_4)_2Cl{\cdot}KCl$ at 8 K.

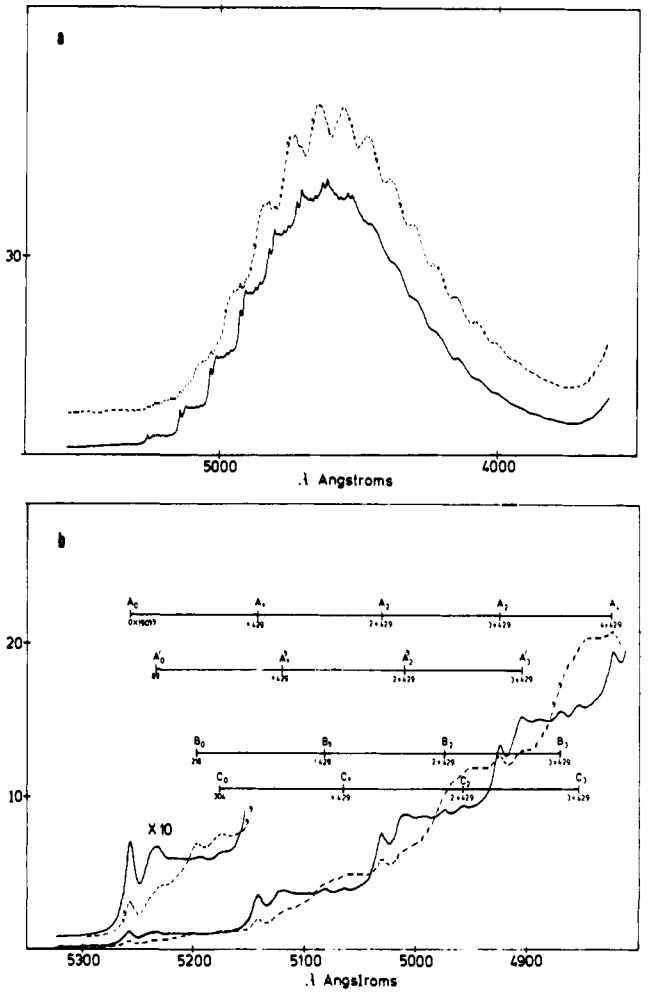

Figure 2. (a) $^1T_{1g} \leftarrow {}^1A_{1g}$ absorption band in $Co(NH_3)_6(ClO_4)_2Cl{\cdot}KCl$ at 8 K: π polarization (solid curve); σ, α polarization (dashed curve). (b) Low-energy region of the $^1T_{1g} \leftarrow {}^1A_{1g}$ absorption band at 8 K: π polarization (solid curve); σ, α polarization (dashed curve). The indicated energy spacings (relative to A_0) are in wavenumbers.

II. Experimental Section

$Co(NH_3)_6Cl_3$ was prepared by the method of Bjerrum and McReynolds.[6] $Co(NH_3)_6(ClO_4)_3$ was precipitated from a saturated aqueous solution of $Co(NH_3)_6Cl_3$ by the addition of concentrated $HClO_4$. Both salts were recrystallized from H_2O for further purification. Single crystals of $Co(NH_3)_6(ClO_4)_2Cl{\cdot}MCl$ (M = K^+, Rb^+, Cs^+, NH_4^+) were prepared by allowing an aqueous solution containing stoichiometric quantities of $Co(NH_3)_6(ClO_4)_3$, $Co(NH_3)_6Cl_3$, and MCl to evaporate slowly in the dark. These crystals are uniaxial[1] (space group $R\bar{3}m$) and grow in plates with large (0001) faces. Optically clear crystals ~10 mm across and ~3 mm thick could be grown by this method. These were oriented using a Vickers M72 polarizing microscope, polished to desired thickness using a wet filter paper technique, and mounted on a copper sample mount for the low-temperature optical absorption experiments. $Co(ND_3)_6(ClO_4)_2Cl{\cdot}KCl$ was prepared by recrystallizing $Co(NH_3)_6(ClO_4)_2Cl{\cdot}KCl$ at least three times from D_2O until IR indicated that deuteration was complete.

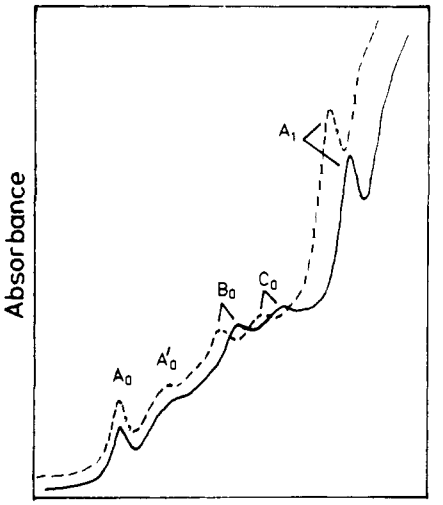

Figure 3. Effects of deuteration on the lowest energy absorption features of the $^1T_{1g} \leftarrow {}^1A_{1g}$ transition: $Co(NH_3)_6(ClO_4)_2Cl{\cdot}KCl$ (solid curve); $Co(ND_3)_6(ClO_4)_2Cl{\cdot}KCl$ (dashed curve).

Low-temperature absorption spectra in the region 3000–8000 Å were obtained using a McPherson RS-10 double beam spectrometer and Janis Super Vari-Temp helium Dewar as previously described.[1] For the absorption experiments in the 8000 Å–1.0 μm region, the extended S-20 response photomultiplier tube was replaced with a dry ice–acetone-cooled S-1 response photomultiplier tube (EMI 9684A). Polarization of the light beam was accomplished using a matched pair of Glan-Taylor calcite prism polarizers which have a spectral range of 2140 Å–2.3 μm.

Low-temperature EPR spectra were obtained using a Varian E9 EPR spectrometer with either the E-245 liquid helium accessory or an Air Products Heli-Tran LTD-3 cryogenic system.

III. $^1T_{1g} \leftarrow {}^1A_{1g}$ Transition

A. Electronic Spectroscopy. The σ, π, and α absorption spectra of the $^1T_{1g} \leftarrow {}^1A_{1g}$ transition (see Figure 1) of $Co(NH_3)_6(ClO_4)_2Cl{\cdot}KCl$ at 6 K are shown in Figures 2a,b. The coincidence of the σ and α spectra shows this band to be electric dipole allowed, which is consistent with the observed loss of integrated intensity upon cooling from room temperature with the transition gaining intensity via a vibronic coupling mechanism. A progression in a 429 ± 3 cm^{-1} mode is clearly visible and is built upon several bands in the low-energy region labeled A_0, A'_0, B_0, and C_0 (Figure 2b). Band A'_0 is a totally symmetric lattice vibration off A_0 as evidenced by its polarization behavior and temperature dependence (vide infra). Upon complete deuteration of the six ammino groups of the $Co(NH_3)_6^{3+}$ chromophore, bands B_0 and C_0 shift to lower energy relative to A_0 (Figure 3). The magnitudes of these shifts are consistent with those found[7] in the ground state for the skeletal modes of the $Co(NH_3)_6^{3+}$ molecule in $Co(NH_3)_6Cl_3$ (Table I). Because of the different polarization behavior of bands B_0 and C_0 with respect to A_0 (Figure 2b), it must be concluded that these are odd parity vibronic origins off the pure electronic *origin* A_0. The vibrational energies suggest an assignment of $\delta(t_{2u})$ and $\delta(t_{1u})$ as the odd parity octahedral normal modes corresponding to the B_0 and C_0 vibronic origins,

Table I

	$\hbar\omega_H$, cm^{-1}	$\hbar\omega_D$, cm^{-1}	$(\hbar\omega_H/\hbar\omega_D)^2$
	$^1T_{1g}$ Energy Spacings Relative to A_0		
A_0	0	0	
A_0'	89	89	1
B_0	218	195	1.22
C_0	304	276	1.21
A_1	429	398	1.16
	$^3T_{1g}$ Energy Spacings Relative to E_0		
E_0	0	0	
E_1[a]	434	397	1.20
E_1[b]	483	453	1.14
	Ground State Vibrational Energies[a]		
$\delta(t_{1u})$	327	292	1.25
$\nu(t_{1u})$	477	436	1.20
$\nu(a_{1g})$	490	460	1.13
$\nu(e_g)$	440	407	1.17
$\delta(t_{2g})$	317	278	1.30

[a] From ref 7.

respectively, with the energies somewhat reduced in the excited state. This assignment is consistent with the observation[1] of similar vibronic origins in the ^2E_g state of $Cr(NH_3)_6^{3+}$.

The coincidence of the σ and α spectra for the pure electronic origin A_0 (Figure 2b) shows that it is electric dipole allowed, which is inconsistent with the g-g nature of the pure electronic transition and the room temperature crystal structure determination[1] which shows the Co^{3+} ion to be at a D_{3d} site (retaining inversion). Figure 4 shows the $^1T_{1g} \leftarrow {}^1A_{1g}$ π absorption spectrum at 220, 54, and 30 K. The total integrated intensity, upon lowering the temperature, first decreases (according to the coth law) and then increases in the 6–50 K range. The increase in total integrated intensity in this temperature range corresponds to the increase in the intensity (with no change in bandwidth) of origin A_0 as shown in Figure 5. This "nonvibronic" temperature-dependent behavior can be understood on the basis of a low temperature induced odd parity low symmetry crystal field at the Co(III) site. This odd parity field allows mixing of higher energy odd parity electronic states into the $^1T_{1g}$ wave function, giving electric dipole intensity to the pure electronic origin.

B. Low-Temperature Co(III) Site Symmetry. In order to proceed with the high-resolution investigations of the $^1T_{1g} \leftarrow {}^1A_{1g}$ and $^3T_{1g} \leftarrow {}^1A_{1g}$ transitions it was necessary to further investigate the symmetry of the low-temperature site. By doping ~0.1% of $Cr(NH_3)_6^{3+}$ into a $Co(NH_3)_6(ClO_4)_2Cl{\cdot}KCl$ single crystal, EPR measurements were made to determine if the low-temperature site retained a threefold axis of symmetry. Following Okumura,[8] the spin Hamiltonian for the $^4A_{2g}$ ground state of $Cr(NH_3)_6^{3+}$ in a lattice site with superimposed axial and rhombic crystal fields is

$$H = \beta(g_x\hat{S}_xH_x + g_y\hat{S}_yH_y + g_z\hat{S}_zH_z) + D[\hat{S}_z^2 - \tfrac{1}{3}S(S+1)] + E(\hat{S}_x^2 - \hat{S}_y^2) \quad (1)$$

where $\hat{S}_x$, $\hat{S}_y$, and $\hat{S}_z$ are spin operators; H_x, H_y, and H_z are components of the magnetic field; D = spin Hamiltonian parameter for the axial field; E = spin Hamiltonian parameter for the rhombic field; $S = \frac{3}{2}$. This spin Hamiltonian operates on the four $|^4A_{2g}S = \frac{3}{2}M_s = \pm\frac{3}{2}, \pm\frac{1}{2}\rangle$ partners of the $^4A_{2g}$ ground state. The magnitude of E measures the departure of the site from axial symmetry where a purely axial environment has $E = 0$. In this case, the magnetic field strength separation between the $\frac{1}{2} \leftrightarrow \frac{3}{2}$ and $-\frac{1}{2} \leftrightarrow -\frac{3}{2}$ transitions is maximum when H is parallel to the unique trigonal axis and equals $4D$. As the crystal is rotated, the unique axis makes an angle θ with respect to the magnetic field. The spin states then mix and the

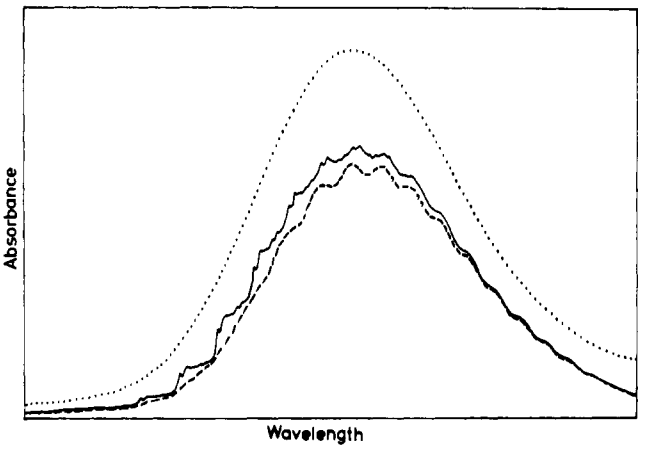

Figure 4. Temperature effects upon the $^1T_{1g} \leftarrow {}^1A_{1g}$ absorption band shape in $Co(NH_3)_6(ClO_4)_2Cl{\cdot}KCl$: 220 (dotted curve); 54 (dashed curve); 30 K (solid curve).

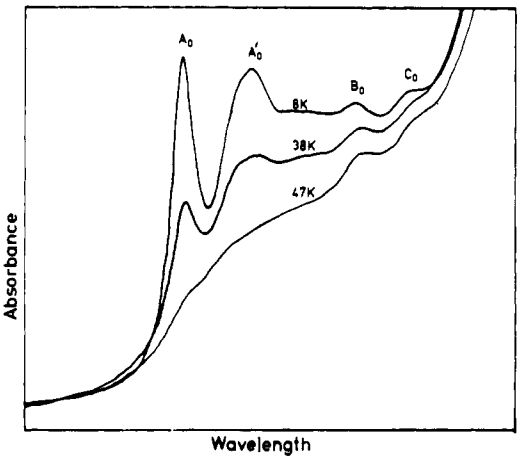

Figure 5. Temperature effects upon the $^1T_{1g} \leftarrow {}^1A_{1g}$ origin region.

transitions corresponding to $\frac{1}{2} \leftrightarrow \frac{3}{2}$ and $-\frac{1}{2} \leftrightarrow -\frac{3}{2}$ approach each other, crossing at $\theta = \cos^{-1}(3^{-1/2}) = 54.74°$. The angle of this crossing position is significantly altered if there is a superimposed nonaxial rhombic field ($E \neq 0$) and a measurement of this angular deviation allows a determination of the E/D ratio. This data for $Cr(NH_3)_6^{3+}$-doped $Co(NH_3)_6(ClO_4)_2Cl{\cdot}KCl$ at 4.2 K is shown in Figure 6, where it is determined that $E/D < 0.002$, thus indicating the retention of the trigonal axis in the low-temperature site. This experiment also shows that all the sites are equivalent as no unaccountable lines in the EPR spectrum were observed.

We can now deduce the nature of the low-temperature site. The EPR results require the site to retain a C_3 axis at all temperatures. Since the room-temperature site is D_{3d}, the electric dipole nature of the origin at 8 K shows the low-temperature site to be a trigonal subgroup of D_{3d} which lacks inversion, limiting the choices to D_3, C_3, and C_{3v}. Because the experimental π/σ intensity ratio is 3.1 (Figure 2b), the subgroup C_{3v} may be eliminated as it would predict no π intensity for the A_0 band. With the data available, it is not possible to distinguish between D_3 or C_3. However, since nothing essential is changed for either choice in the following analysis, we take the low-symmetry site to be D_3. A D_3 site symmetry assignment is supported by a calculation of the relative σ and π intensities of the $^1T_{1g} \leftarrow {}^1A_{1g}$ transition using the irreducible tensor method of Tanabe, Sugano, and Kamimura.[9] Here an effective electric dipole transition moment operator may be written for the situation where an odd parity D_3 crystal field induces intensity into the $^1T_{1g} \leftarrow {}^1A_{1g}$ transition. The effective

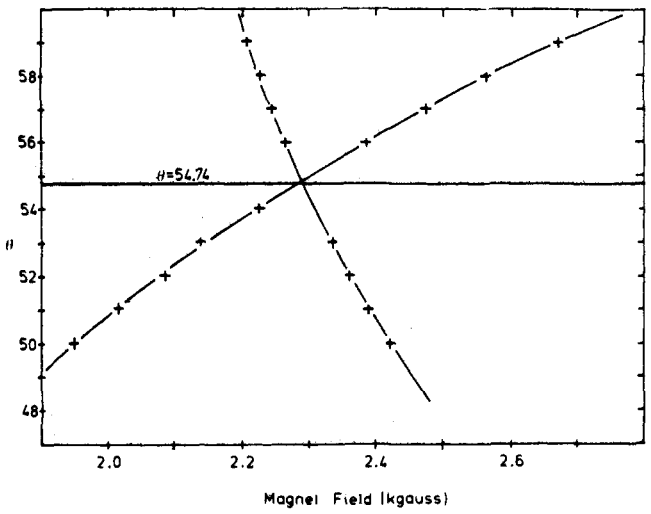

Figure 6. Plot of the magnetic field position of the $\frac{1}{2} \leftrightarrow \frac{3}{2}$ and $-\frac{1}{2} \leftrightarrow -\frac{3}{2}$ transitions vs. θ for the $^4A_{2g}$ ground state of 0.1% $Cr(NH_3)_6^{3+}$ doped into $Co(NH_3)_6(ClO_4)_2Cl{\cdot}KCl$ at 4.2 K. The horizontal line at $\theta = 54.74$ represents the angle at which these transitions "cross" in a purely axial crystal field.

moment operator is expressed as a linear combination of octahedral irreducible tensor operators as follows:

$$P_0^{\text{eff}} = \frac{-1}{\sqrt{3}} W(A_{2g}) + \frac{\sqrt{2}}{\sqrt{3}} W_{a0}(T_{1g}) \qquad (2)$$

$$P_+^{\text{eff}} = \frac{-i}{\sqrt{3}} W_{u+}(E_g) - \frac{1}{\sqrt{6}} W_{a+}(T_{1g}) - \frac{i}{\sqrt{2}} W_{x+}(T_{2g})$$

where $W_\gamma(\Gamma)$ is the γth partner of the irreducible tensor operator of symmetry species Γ in a trigonal basis (nomenclature from ref 9), P_0^{eff} is the effective moment operator for π polarization, and P_+^{eff} is the effective moment operator for σ polarization.

Using the Wigner-Eckart theorem, the matrix elements of these operators are evaluated between the $|^1A_{1g}\rangle$, $|^1T_{1g}\gamma\rangle$ states in a trigonal basis giving a predicted polarization ratio for band A_0 of

$$\frac{I_\pi}{I_\sigma} = \frac{|\langle {}^1A_{1g}|P_0|{}^1T_{1g}a_0\rangle|^2}{|\langle {}^1A_{1g}|P_+|{}^1T_{1g}a_-\rangle|^2} = 4.0 \qquad (3)$$

This compares favorably with the experimentally obtained value of $I_\pi/I_\sigma = 3.1$. Since the above calculation relies only on symmetry and the assumption of closure over high-lying odd parity states it provides additional support for an approximate D_3 low-temperature site symmetry at the Co(III) ion.

C. Franck-Condon Analysis and Excited-State Geometry. We now use the temperature dependence of the pure electronic origin to determine the Huang-Rhys parameters defined by

$$S = \tfrac{1}{2}k(\Delta Q)^2/\hbar\omega \qquad (4)$$

where ΔQ is the excited-state distortion in a vibrational mode Q having force constant k and frequency ω for the 429-cm^{-1} progressional mode. The intensity of the first progressional member with respect to the pure electronic origin is given by the expression

$$I_1 = SI_0 \qquad (5)$$

Thus a plot of I_1 vs I_0 for different values of temperature produces a straight line with a slope equal to the Huang-Rhys parameter S. The I_1 intercept indicates the amount of overlap between the I_0 and I_1 regions. The plot of the peak height of A_1 vs. A_0 for different values of temperature is shown in Figure 7, and gives a value of $S = 2.8 \pm 0.1$ for the 429-cm^{-1} progressional mode.

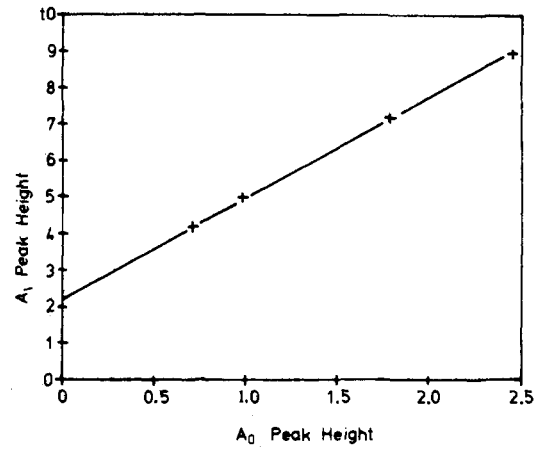

Figure 7. Plot of the peak heights (arbitrary units) of A_1 vs. A_0. A least-squares fit gives a slope of 2.8 ± 0.1 and an A_1 intercept of 22.

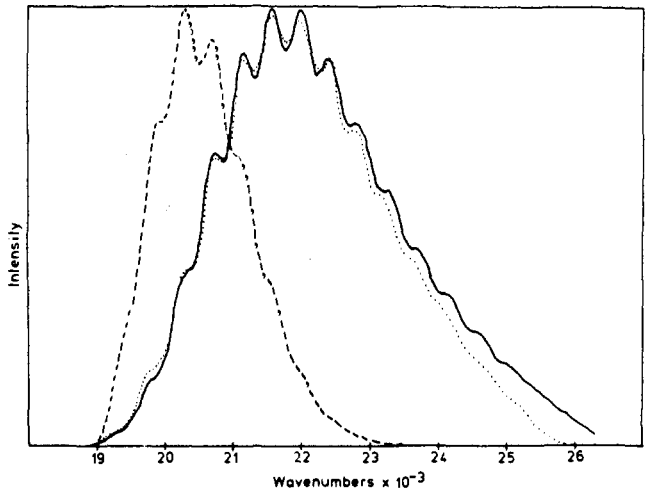

Figure 8. Comparison of the experimental (solid curve) $^1T_{1g} \leftarrow {}^1A_{1g}$ band shape with the calculated band shape for $S = 2.8$, $\hbar\omega = 429$ cm^{-1} (dashed curve), and $S_1 = 2.8$, $\hbar\omega_1 = 429$ cm^{-1}, $S_2 = 3.6$, $\hbar\omega_2 = 480$ cm^{-1} (dotted curve).

Using the experimentally obtained I_0 region (A_0, A'_0, B_0, C_0) and the parameters $\hbar\omega = 429$ and $S = 2.8$, we can now generate a predicted band shape for the $^1T_{1g} \leftarrow {}^1A_{1g}$ transition using the expression

$$I(E) = \sum_{n=0} e^{-s} \frac{S^n}{n!} g_0(E - n\hbar\omega) \qquad (6)$$

where g_0 is the function representing the experimentally observed I_0 region and n is the vibrational quantum number in the progressional mode. It is seen in Figure 8 that the 429-cm^{-1} progressional mode alone is insufficient to account for the whole $^1T_{1g} \leftarrow {}^1A_{1g}$ absorption band shape. This requires the existence of an additional molecular progressional mode. We determine this additional mode by least-squares fitting the experimental $^1T_{1g} \leftarrow {}^1A_{1g}$ band shape to an expression of the form

$$I(E) = \sum_{n_1} \sum_{n_2} e^{-s_1-s_2} \frac{S_1^{n_1} S_2^{n_2}}{n_1! n_2!} g_0(E - n_1\hbar\omega_1 - n_2\hbar\omega_2) \qquad (7)$$

By fixing $S_1 = 2.8$ and $\hbar\omega_1 = 429$ (from the preceding analysis of the origin region), we then allow $\hbar\omega_2$ and S_2 to vary until a best fit is achieved (Figure 8). From this we obtain the parameters $S_2 = 3.6$ and $\hbar\omega_2 = 480$. Group theory predicts the possible progressional modes of the CoN_6 octahedron to be a_{1g}, e_g, and t_{2g}. These are the normal modes along which an excited state of T_{1g} orbital symmetry may undergo a distortion. Be-

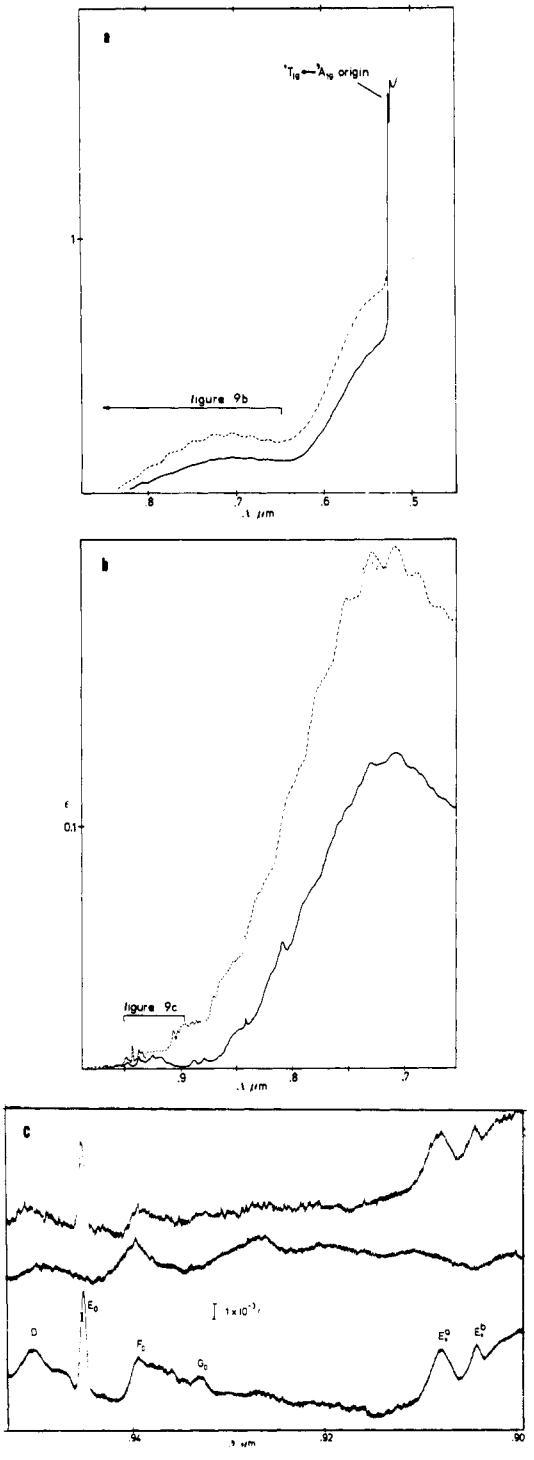

Figure 9. (a) Absorption spectrum of $Co(NH_3)_6(ClO_4)_2Cl{\cdot}KCl$ at 8 K showing the origin of the $^1T_{1g} \leftarrow {}^1A_{1g}$ transition, and the weaker, lower energy $^3T_{2g} \leftarrow {}^1A_{1g}$, $^3T_{1g} \leftarrow {}^1A_{1g}$ transition: π polarization (solid curve); σ, α polarization (dashed curve). (b) Further magnification of the overall $^3T_{1g} \leftarrow {}^1A_{1g}$ transition with visible origin region: π polarization (solid curve); σ, α polarization (dashed durve). (c) Origin region of the $^3T_{1g} \leftarrow {}^1A_{1g}$ transition in $Co(NH_3)_6(ClO_4)_2Cl{\cdot}KCl$ at 8 K. σ, π, and α polarizations are indicated.

cause the t_{2g} vibrational energy is $\sim$300 cm^{-1} in the ground state,[7] the observed progressions cannot be assigned to this mode. The ground-state vibrational energies for $\nu(a_{1g})$ and $\nu(e_g)$ are 490 and 440 cm^{-1}, respectively. Hence we assign the 480-cm^{-1} progressional mode as $\nu(a_{1g})$ and the 429-cm^{-1} progressional mode as $\nu(e_g)$, both somewhat reduced in energy in the excited state. The $^1T_{1g}$ state undergoes a reasonably large e_g Jahn-Teller effect ($S_{e_g} = 2.8$) which explains why no

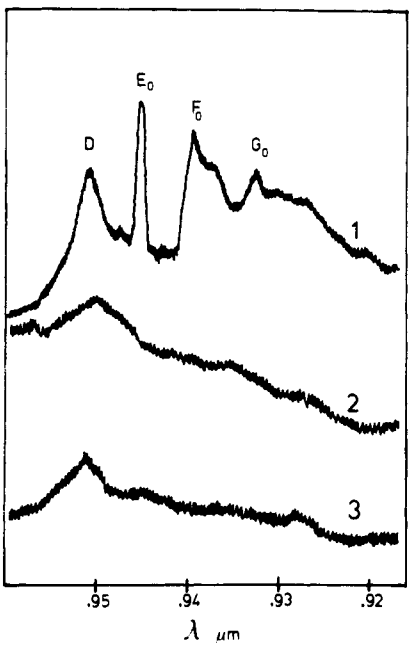

Figure 10. Comparison of 0.92–0.96-μm spectral region of $Co(NH_3)_6(ClO_4)_2Cl{\cdot}KCl$ (curve 1), $Cr(NH_3)_6(ClO_4)_2Cl{\cdot}KCl$ (curve 2), and $Co(NH_3)_6(ClO_4)_2Cl{\cdot}CsCl$ (curve 3) at 8 K in the σ polarization.

first-order trigonal splitting is observed in the pure electronic origin as this splitting would be quenched by the Ham effect (see section IVC).

IV. $^3T_{1g} \leftarrow {}^1A_{1g}$ Transition

A. Electronic Spectroscopy. Figures 9a–c present the $^3T_{1g} \leftarrow {}^1A_{1g}$ transition with increasing sensitivity and higher resolution in the low-energy origin region (Figure 9c). Note that the ϵ scale is a factor of $\sim 10^4$ more sensitive than that of Figure 2a for the $^1T_{1g} \leftarrow {}^1A_{1g}$ transition and represents the first high-resolution data obtained for the $^3T_{1g} \leftarrow {}^1A_{1g}$ transition in a low-spin d^6 complex. This is a particularly complicated spectral region to assign owing to possible absorption contributions from impurities and ground-state N–H overtones which may overlap the electronic transitions to the $^3T_{1g}$ state. Thus a careful investigation of this region was required in order to identify and assign the structure associated with the $^3T_{1g} \leftarrow {}^1A_{1g}$ transition.

As seen in Figure 9c, the correspondence between the σ and α spectra reveal that all structure in this region is electric dipole allowed, which is consistent with the results previously obtained for the $^1T_{1g} \leftarrow {}^1A_{1g}$ transition (section III). Next, a comparison of this region with the corresponding region of $Cr(NH_3)_6(ClO_4)_2Cl{\cdot}KCl$ (which has no electronic transition below 15 190 cm^{-1}) demonstrates (Figure 10) that only band D (and several other weaker features toward higher energy which will not be discussed further) is an ammine hydrogen overtone (or combination) of the ground state. We eliminate the possibility of impurities from a comparison (Figure 10) of the spectra of two $Co(NH_3)_6(ClO_4)_2Cl{\cdot}MCl$ salts, made with the same cobalt starting material but different cation compound. The sharp structure is seen to be present only for the K salt, consistent with the low-temperature odd parity site present in this lattice which induces intensity into the sharp origins.

Further, the effects of temperature on this structure (Figure 11) exactly parallel the effects observed in the origin region of the $^1T_{1g} \leftarrow {}^1A_{1g}$ transition. Therefore, it is clear that bands E_0, F_0, G_0, E_1^a, and E_1^b must be associated with the pure electronic origins (or totally symmetric vibrations built on those origins) rather than odd-parity vibronic origins or the extra-

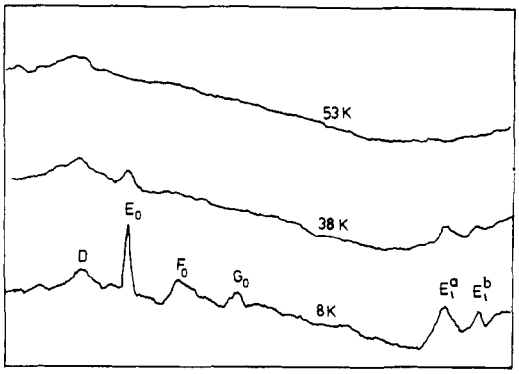

Figure 11. Effects of temperature on bands in the origin region of the $^3T_{1g} \leftarrow {}^1A_{1g}$ transition in $Co(NH_3)_6(ClO_4)_2Cl{\cdot}KCl$.

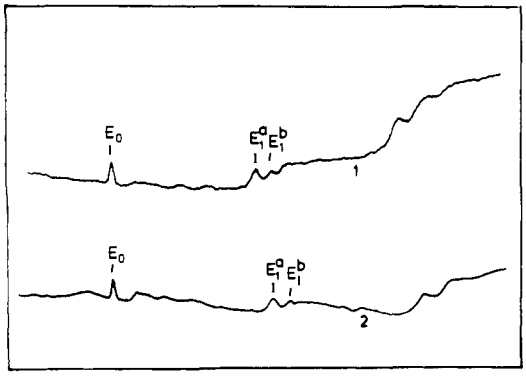

Figure 12. Effects of deuteration on the E_1^a, E_1^b bands in $Co(NH_3)_6(ClO_4)_2Cl{\cdot}KCl$ at 8 K. The E_0 band of the deuterated salt (curve 1) is superimposed on the E_0 band of the undeuterated salt (curve 2).

neous effects just discussed. We next identify the different electronic origins and totally symmetric vibrations built upon these for comparison with the theoretical treatment in the following sections. Bands E_0 and F_0 are seen to have different σ and π polarizations (Figure 9c; E_0 is pure σ while F_0 is σ and π) and thus must be assigned as different electronic origins. Next, although it is possible that G_0 may be a low-energy totally symmetric progression on E_0, no corresponding band is observed in the $^1T_{1g}$, nor is there a corresponding progression off F_0. Deuteration of the ammines (Figure 12 and Table I) shows that bands E_1^a and E_1^b are shifted with respect to E_0 by amounts consistent with those observed for skeletal modes in the ground state. This data, taken together with their having the same pure σ polarization behavior as E_0, requires E_1^a, E_1^b to be progressional modes built upon E_0. In parallel to our results in the $^1T_{1g} \leftarrow {}^1A_{1g}$ transition (the $^3T_{1g}$ and $^1T_{1g}$ states have the same $t_{2g}^5e_g$ electronic configuration and orbital symmetry), we assign band E_1^a as $\nu(e_g)$ and E_1^b as $\nu(a_{1g})$. In summary, bands E_0, F_0, and probably G_0 are the pure electronic origins of the $^3T_{1g}$ spin-orbit multiplet and bands E_1^a and E_1^b are the first progressional members in the $\nu(e_g)$ and $\nu(a_{1g})$ modes, respectively, built upon origin E_0.

B. Franck-Condon Analysis and Excited-State Geometry. Having determined that E_1^a and E_1^b are the first members of the $\nu(e_g)$ and $\nu(a_{1g})$ progressional modes built upon origin E_0, we can now determine the Huang-Rhys parameters $S_{a_{1g}}$ and S_{e_g} for the $^3T_{1g}$ state. The intensity of the n_1th, n_2th progressional member is proportional to the factor

$$I(n_1,n_2) \propto \exp(-S_{a_{1g}} - S_{e_g}) \frac{S_{a_{1g}}{}^{n_1} S_{e_g}{}^{n_2}}{n_1! n_2!} \qquad (8)$$

where n_1 and n_2 are the number of quanta in the $\nu(a_{1g})$ and $\nu(e_g)$ modes, respectively. Thus the intensity ratio between the first progressional members in each mode is given as

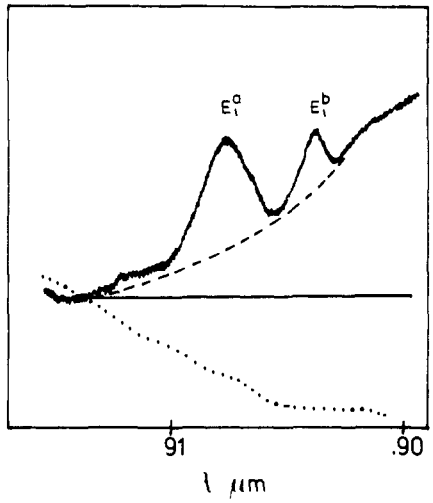

Figure 13. Three possible base lines used for the determination of the $I(0,1)/I(1,0)$ ratio. The dashed line (case a) corresponds to a sloping continuation of the spectrum to higher energy (<0.903 μm). The solid line (case b) corresponds to an extrapolation of zero intensity at 0.915 μm. The dotted line (case c) corresponds to the base line obtained from an equally thick crystal of $Cr(NH_3)_6(ClO_4)_2Cl{\cdot}KCl$ in the same spectral region.

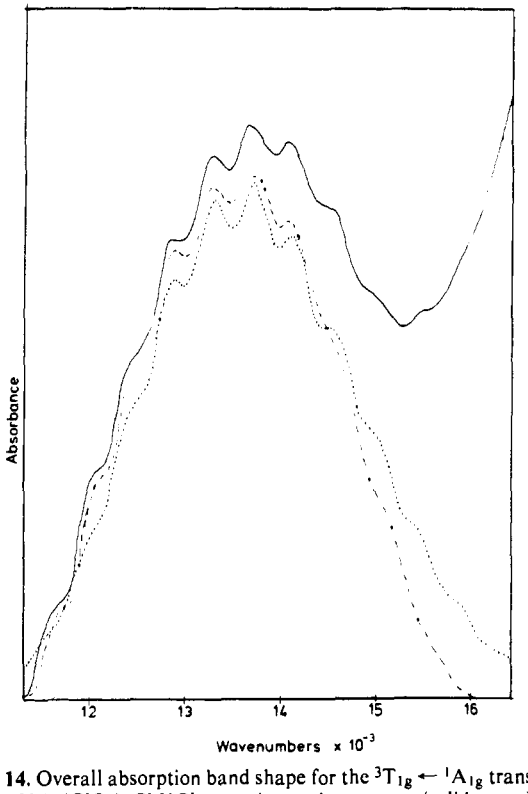

Figure 14. Overall absorption band shape for the $^3T_{1g} \leftarrow {}^1A_{1g}$ transition in $Co(NH_3)_6(ClO_4)_2Cl{\cdot}KCl$: experimental spectrum (solid curve); experimental spectrum corrected for overlap with $^1T_{1g} \leftarrow {}^1A_{1g}$, $^3T_{2g} \leftarrow {}^1A_{1g}$ transitions (dashed curve); calculated band shape with $S_{a_{1g}} + S_{e_g} = 6.1$ and $\hbar\omega = (434 + 483)/2$ (dotted curve).

$$I(0,1)/I(1,0) = S_{e_g}/S_{a_{1g}} \qquad (9)$$

Because of the overlap of the E_1^a ($I(0,1)$ and E_1^b ($I(1,0)$) bands and because of ambiguities in the base line in this spectral region, this ratio can only be determined approximately as shown in Figure 13. Here, three possibilities (a-c) for the separation of $I(0,1)$ and $I(1,0)$ are considered. In all cases $I(0,1) > I(1,0)$. We determine the sum $S_{a_{1g}} + S_{e_g}$ from a least-squares fit (assuming one effective progressional mode) to the overall band shape which has been corrected for overlap with the $^3T_{2g}$ and $^1T_{1g}$ absorption bands (Figure 14). Within the framework

Table II. Possible Values of the Huang-Rhys Parameters $S_{a_{1g}}$ and S_{e_g} for $^3T_{1g}$[a]

case	$S_{e_g}/S_{a_{1g}}$	$S_{a_{1g}}$	S_{e_g}	$S_{a_{1g}} + S_{e_g}$
a	2.81	1.6	4.5	6.1
b	1.54	2.4	3.7	6.1
c	1.18	2.8	3.3	6.1

[a] See Figure 13.

of the Huang-Rhys approximation (several progressional modes of equal frequency) this procedure has been shown[1,10] to yield the sum of the Huang-Rhys parameters for the progressional modes generating the band shape. Using this result and the $I(0,1)/I(1,0)$ ratios determined in Figure 13, we obtain $S_{a_{1g}}$ and S_{e_g} as shown in Table II. We proceed using representative values from the intermediate case b: $S_{a_{1g}} = 2.4 \pm 0.8$; $S_{e_g} = 3.7 \pm 0.8$.

C. Electronic Splittings of the $^3T_{1g}$ Origins and Jahn-Teller Effect. We now consider the Hamiltonian for $Co(NH_3)_6^{3+}$ in a D_3 site:

$$H = H_{FI} + H_{OCT} + H_{SO} + H_{VIB} + H_{D_3} \qquad (10)$$

The first two terms representing the free ion and octahedral crystal field are solved using the complete Tanabe and Sugano matrices[11] to give the crystal-field terms $|^{2S+1}\Gamma\rangle$. The parameters Dq, B, and C are determined by an iterative procedure in which these parameters are systematically adjusted until computer diagonalization of the complete matrices gives the experimentally determined $^3T_{1g} \leftarrow {}^1A_{1g}$, $^1T_{1g} \leftarrow {}^1A_{1g}$, and $^1T_{2g} \leftarrow {}^1A_{1g}$ absorption band maxima energies to within 1 cm^{-1}. These energies represent the energy of the "vertical" transition between the lowest ground vibronic level and the excited-state potential surface. The next term, H_{SO}, the spin-orbit interaction, splits the ninefold degenerate $|^3T_{1g}\rangle$ term into four levels transforming as Γ_1, Γ_3, Γ_4, and Γ_5 (Bethe notation) in the octahedral double group. We take account of the spin-orbit interaction using an effective Hamiltonian which operates on the nine partners ($|^3T_{1g}\bar{\gamma}M_s\rangle$, $\bar{\gamma} = \alpha, \beta, \gamma$; $M_s = 0, \pm 1$) of the $^3T_{1g}$ state. The effective spin-orbit Hamiltonian has the form[12]

$$H_{SO}^{eff} = \lambda \mathbf{L}\cdot\mathbf{S} + \kappa(\mathbf{L}\cdot\mathbf{S})^2 + \rho(L_x^2 S_x^2 + L_y^2 S_y^2 + L_z^2 S_z^2) \qquad (11)$$

The term in λ gives primarily the first-order splitting, while the terms in κ and ρ come only from second-order contributions, the ρ term inducing the octahedral symmetry and splitting the Γ_3, Γ_5 pair. The values of λ, κ, and ρ are determined by diagonalizing the effective Hamiltonian and fitting the energy solutions to a second-order calculation using the complete d^4 spin-orbit matrices of Schroeder.[13] These matrices are used for d^6 by changing the sign of the matrix elements. The covalency-reduced one-electron spin-orbit coupling constant ζ is unknown, but has been estimated[14] to be in the range of 500-600 cm^{-1}. Here we take $\zeta = 600$ cm^{-1} to represent an upper limit of the $^3T_{1g}$ multiplet splittings.

Since we are interested in the spin-orbit splitting of the lowest vibronic level in the equilibrium geometry of the $^3T_{1g}$ excited state, we must be careful of our choice of energy denominators in the second-order calculation for nearby states ($^1T_{2g}$, $^1T_{1g}$, $^3T_{2g}$, $^1A_{1g}$, $^5T_{2g}$). Because the $^3T_{2g}$, $^1T_{1g}$, and $^1T_{2g}$ states are all orbital triplets and derive from the same electronic configuration as the $^3T_{1g}$ state, these states are all expected to have similar excited-state potential surfaces. This assumption is borne out by the similarity of the Huang-Rhys parameters and vibrational energies in the $^1T_{1g}$ and $^3T_{1g}$ excited states (sections IIIC and IVB). This means that energy denominators determined experimentally from band maxima in absorption for these states will be, to a good approximation, valid for the equilibrium geometry as well. For the ground state, however, each vibronic level will give a different second-order contribution to the Γ_1 component of the $^3T_{1g}$ multiplet, the summation over all vibronic levels being

$$E^{(2)}(\Gamma_1\,{}^1A_{1g}) = \sum_{n_1 n_2} \frac{|\langle {}^3T_{1g}\Gamma_1 00|H_{SO}|{}^1A_{1g}\Gamma_1 n_1 n_2\rangle|^2}{E_{00} - n_1\hbar\omega_{a_{1g}} - n_2\hbar\omega_{e_g}}$$

$$= |\langle {}^3T_{1g}\Gamma_1|H_{SO}|{}^1A_{1g}\Gamma_1\rangle|^2 \Sigma \frac{e^{-S_{a_{1g}}-S_{e_g}} S_{a_{1g}}{}^{n_1} S_{e_g}{}^{n_2}/n_1!n_2!}{E_{00} - n_1\hbar\omega_{a_{1g}} - n_2\hbar\omega_{e_g}} \qquad (12)$$

The sum over n_1 and n_2 is evaluated using the experimentally derived values of $S_{a_{1g}}$, S_{e_g}, $\hbar\omega_{a_{1g}}$, $\hbar\omega_{e_g}$, and E_{00} is taken to be 10 579 cm^{-1}. The $^5T_{2g}$ state is predicted from the Tanabe-Sugano calculations to lie 3634 cm^{-1} above the $^3T_{1g}$ state in the ground-state equilibrium geometry. For our initial treatment then, we assumed closure over the vibronic levels of the $^5T_{2g}$ state and use this value for the energy denominator in the second-order expressions. However, in the analysis to follow, we will find that the observed $^3T_{1g}$ origin splittings are extremely sensitive to the position of the $^5T_{2g}$. These effects must then be considered in detail in section V. For the higher excited states, energy denominators were determined from the solutions to the Tanabe-Sugano matrices with no further corrections. The parameters Dq, B, C, λ, κ, and ρ determined as described above are collected in Table III.

Table III. Effective Hamiltonian Parameters

$Dq = 2400$ cm^{-1}	$\lambda = -160$
$B = 619$ cm^{-1}	$\kappa = +73$
$C = 3656$ cm^{-1}	$\rho = -27$

We can now include the term H_{vib} in our effective Hamiltonian for the $^3T_{1g}$ state. This requires our wave functions to be a product of an electronic and a vibrational part (Born-Oppenheimer approximation). We have already anticipated this in our treatment of the second-order spin-orbit contribution from the ground state. For a given value of M_s, H_{vib} within the $|^3T_{1g}\bar{\gamma}M_s\rangle$ basis ($\bar{\gamma} = \alpha, \beta, \gamma$) is given by the expression[15]

$$H_{vib}^{eff} = \sum_i \frac{P_i^2}{2\mu_i} + \tfrac{1}{2}k_i Q_i^2$$

$$+ \left\langle {}^3T_{1g}\left|\left|\frac{\partial V}{\partial Q_{a_{1g}}}\right|\right|{}^3T_{1g}\right\rangle \begin{bmatrix} Q_{a_{1g}} & 0 & 0 \\ 0 & Q_{a_{1g}} & 0 \\ 0 & 0 & Q_{a_{1g}} \end{bmatrix}$$

$$+ \left\langle {}^3T_{1g}\left|\left|\frac{\partial V}{\partial Q_{e_g}}\right|\right|{}^3T_{1g}\right\rangle$$

$$\times \begin{bmatrix} -\tfrac{1}{2}Q_u + \frac{\sqrt{3}}{2}Q_v & 0 & 0 \\ 0 & -\tfrac{1}{2}Q_u - \frac{\sqrt{3}}{2}Q_v & 0 \\ 0 & 0 & Q_u \end{bmatrix} \qquad (13)$$

where the notation and phases are those of Tanabe, Sugano, and Kamimura.[9]

These terms convert the $^3T_{1g}$ energy level into a potential-energy surface with an associated manifold of vibronic states. The linear term in $Q_{a_{1g}}$ displaces the equilibrium position (relative to the ground state) of each orbital partner equally in the same direction along the $Q_{a_{1g}}$ coordinate (see Figure 6a, ref 1). The linear term in Q_{e_g} displaces the equilibrium position of each orbital partner equally but along different directions in the doubly degenerate Q_{e_g} space (see Figure 6b, ref 1). This inequivalent displacement of the T_1 orbital partners in the $e_g u$,

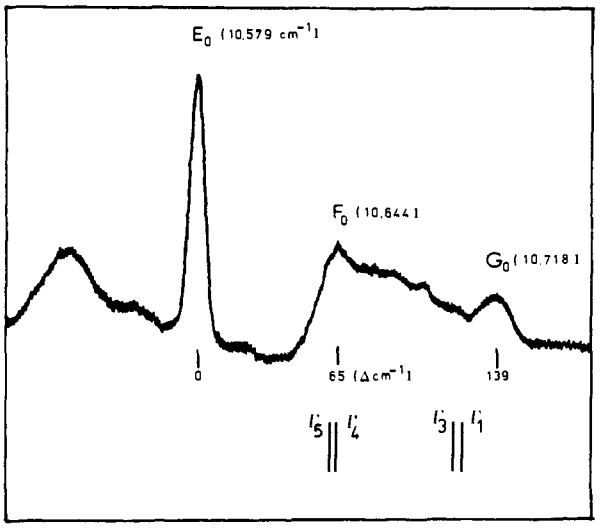

Figure 15. Pure electronic origin of the $^3T_{1g} \leftarrow {}^1A_{1g}$ transition (σ polarization) and superimposed calculated energy solutions to the effective Hamiltonian. The Γ_4 component is aligned with F_0 based on the spectral assignment.

$e_g\upsilon$ coordinate space reduces matrix elements of purely electronic operators connecting different orbital partners. These will be multiplied by a vibrational overlap factor, which for the 00 level (purely electronic) of the $^3T_{1g}$ state is the Ham[16] reduction factor

$$R^{\text{Ham}} = e^{-3/2)S_{e_g}} \tag{14}$$

where S_{e_g} was obtained experimentally as $S_{e_g} = 3.7$ in section IVB.

The first-order splitting of the spin-orbit coupling given by the term $\lambda \mathbf{L}\cdot\mathbf{S}$ is completely off-diagonal and is therefore greatly reduced in magnitude by the reduction factor (Ham effect). The term H_{D_3} is also completely off-diagonal and since it is a small term to begin with (being an outer-coordination sphere effect) the Ham effect makes it completely negligible and we may neglect its effect on the electronic energies. However, H_{D_3} still exerts its influence on the intensities and polarizations of the electronic transitions as these are out-of-state effects. Thus we expect to observe the polarizations we would have had in the absence of a Ham effect, but with no trigonal splitting of the polarized components. A similar behavior was observed (section III) for the electronic origin of the $^1T_{1g}$ state. In Table IV we present the selection rules for the spin-orbit components of the $^3T_{1g}$ state. From the table we expect to observe two purely σ-polarized bands corresponding to the Γ_3 and $\Gamma_5(O_h)$ spin-orbit components and one $\sigma\pi$ polarized band corresponding to the Γ_4 spin-orbit component. These predictions are in good agreement with the spectroscopic results, where we have already determined (section IVA) that bands $E_0(\sigma)$, $F_0(\sigma$ and $\pi)$, and $G_0(\sigma)$ (Figure 9c) must be assigned as the pure electronic origins of the $^3T_{1g}$ state. Band F_0 may then be unambiguously identified as the Γ_4 component from its polarization behavior, although part of its σ intensity probably derives from an overlapping totally symmetric lattice mode (A_0' in Figure 5) built upon E_0. Finally, although the assignment of F_0 (as Γ_4) is clear, the present data does not allow us to decide which σ-polarized band (E_0, G_0) is to be associated with which of the remaining spin-orbit components (Γ_3 or Γ_5).

We now solve the complete effective Hamiltonian for the $^3T_{1g}$ state taking all nonnegligible terms described in eq 10, 11, and 14 into account. The results of this calculation are shown in Figure 15, where we have superimposed the experimental spectrum, correlating the Γ_4's. We note the inconsistency between experiment and theory as it is not possible to predict the observed splitting pattern of polarized bands within the error bars of the parameters used in the calculation. Since the theory and approach used here have been successfully applied in a number of similar studies[1,12,17] reasonable agreement is to be expected. This disagreement is due to the sensitivity of the origin region to the effects of the nearby strongly perturbing $^5T_{2g}$ state which interacts with the $^3T_{1g}$ state through spin-orbit coupling. This interaction is discussed in section V.

Table IV. D_3 Selection Rules

O_h	D_3	polarization
Γ_1	Γ_1	forbidden
Γ_3	Γ_3	σ
Γ_4	$\Gamma_2 + \Gamma_3$	$\pi\sigma$
Γ_5	$\Gamma_1 + \Gamma_3$	σ

V. $^3T_{1g}$–$^5T_{2g}$ Interaction and the $^5T_{2g}$ Potential Energy Surface

In section IVC we took into account the effect of the $^3T_{1g}$–$^5T_{2g}$ spin-orbit interaction on the multiplet splittings of the lowest vibronic level of the $^3T_{1g}$ state through a second-order term of the form

$$E^{(2)}(^3T_{1g}\Gamma) = \frac{|\langle {}^3T_{1g}\Gamma|H_{SO}|{}^5T_{2g}\Gamma\rangle|^2}{E(^3T_{1g}) - E(^5T_{2g})} \tag{15}$$

where $E(^3T_{1g})$ and $E(^5T_{2g})$ are the energies calculated from computer diagonalization of the Tanabe and Sugano matrices. This calculation predicts the $^5T_{2g}$ state to lie some 3600 cm^{-1} above the $^3T_{1g}$ state in the $^1A_{1g}$ ground-state equilibrium geometry.

We found poor agreement between the theory at this level and the experimentally determined splittings of the $^3T_{1g}$ origins. This is due to the close proximity of the $^5T_{2g}$ state and the fact that large differences are to be expected between the $^3T_{1g}$ and $^5T_{2g}$ potential energy surfaces, the quintet resulting from a two-electron excited configuration ($t_{2g}^4e_g^2$). At the equilibrium geometry of the triplet, the situation appropriate for the $^3T_{1g}$ origin calculation, the relative energies of the two states should then be quite different from the 3600-cm^{-1} value used above. We now consider in some detail the effects of variation of the $^5T_{2g}$ position relative to the $^3T_{1g}$ on the latter's electronic origin splittings and use the experimentally observed triplet splittings to fix the approximate position of the quintet.

For this calculation, it is convenient to use a real basis for both the $^3T_{1g}$ and $^5T_{2g}$ states. The matrix elements of the spin-orbit operator between the $n_1 = 0$, $n_2 = 0$ level of the $^3T_{1g}$ state and the n_1th, n_2th level of the $^5T_{2g}$ state are then

$$\langle {}^3T_{1g}\gamma' M_s' 00|H_{SO}|{}^5T_{2g}\gamma'' M_s'' n_1 n_2\rangle = \langle {}^3T_{1g}\gamma' M_s'|H_{SO}|{}^5T_{2g}\gamma'' M_s''\rangle\langle\gamma' 00|\gamma'' n_1 n_2\rangle \tag{16a}$$

where $\gamma' = \alpha, \beta, \gamma$; $\gamma'' = \xi, \eta, \zeta$; $M_s' = 0, \pm1$; $M_s'' = 0, \pm1, \pm2$; and $\langle\gamma' 00|\gamma'' n_1 n_2\rangle$ is the overlap integral between the vibrational wave functions for the a_{1g} and e_g modes in the Born-Oppenheimer $|{}^3T_{1g}\gamma' M_s' 00\rangle$ and $|{}^5T_{2g}\gamma'' M_s'' n_1 n_2\rangle$ basis. These matrix elements constitute the off-diagonal block of the $^3T_{1g}$–$^5T_{2g}$ spin-orbit Hamiltonian matrix. Similar expressions exist for the $^3T_{1g}$ diagonal block:

$$\begin{aligned}\langle {}^3T_{1g}\gamma' M_s' 00|\bar{H}_{SO}^{\text{eff}}|{}^3T_{1g}\gamma'' M_s'' 00\rangle &= \langle {}^3T_{1g}\gamma' M_s'|\bar{H}_{SO}^{\text{eff}}|{}^3T_{1g}\gamma'' M_s''\rangle\langle\gamma' 00|\gamma'' 00\rangle \\ &= \langle {}^3T_{1g}\gamma' M_s'|\bar{H}_{SO}^{\text{eff}}|{}^3T_{1g}\gamma'' M_s''\rangle[(1 - \delta_{\gamma'\gamma''})R^{\text{Ham}} + \delta_{\gamma'\gamma''}]\end{aligned} \tag{16b}$$

where γ' and $\gamma'' = \alpha, \beta, \gamma$; M_s' and $M_s'' = 0, \pm1$; $\bar{H}_{SO}^{\text{eff}} =$

effective Hamiltonian without the $^5T_{2g}$ second-order terms; and R^{Ham} = Ham reduction factor. Then for the $^5T_{2g}$ diagonal block we have

$$\langle {}^5T_{2g}\gamma' M_s' n_1' n_2' | H_{SO} | {}^5T_{2g}\gamma'' M_s'' n_1'' n_2'' \rangle = \langle {}^5T_{2g}\gamma' M_s' | H_{SO} | {}^5T_{2g}\gamma'' M_s'' \rangle \langle n_1' n_2' | n_1'' n_2'' \rangle + (\Delta_{00} + n_1'\hbar\omega_{a_{1g}} + n_2'\hbar\omega_{e_g})\delta_{\gamma'\gamma''}\delta_{M_s'M_s''}\delta_{n_1'n_1''}\delta_{n_2'n_2''} \quad (16c)$$

where γ' and $\gamma'' = \xi, \eta, \zeta$; M_s' and $M_s'' = 0, \pm1, \pm2$; Δ_{00} = energy difference between $^5T_{2g}(0,0)$ and $^3T_{1g}(0,0)$ multiplet "center of gravities"; and the vibrational energy has been added along the diagonal.

In order to evaluate the vibrational overlap integral in (16a), it is necessary to determine the relative equilibrium geometries of the $^3T_{1g}$ and $^5T_{2g}$ potential surfaces. Since the Huang-Rhys parameters are unknown for the $^5T_{2g}$ state, we resort to ligand field theory in order to obtain an estimate of these parameters. The $^5T_{2g}$ state derives from the $t_{2g}^4e_g^2$ electronic configuration and is obtained by coupling the $t_{2g}^4(^3T_{1g})$ and $e_g^2(^3A_{2g})$ wave functions. The distorting forces along the e_g and t_{2g} normal coordinates in this state with respect to the $^1A_{1g}$ ground state are given[1] in terms of the one-electron wave functions as

$$F_{e_g}{}^{5T_{2g}} - F_{e_g}{}^{1A_{1g}} = -\left\langle {}^5T_{2g}\zeta M_s \left| \left(\frac{\partial V}{\partial Q_{e_g u}}\right)_0 \right| {}^5T_{2g}\zeta M_s \right\rangle + \left\langle {}^1A_{1g} \left| \left(\frac{\partial V}{\partial Q_{e_g u}}\right)_0 \right| {}^1A_{1g} \right\rangle$$
$$= -\left\langle u \left| \left(\frac{\partial V}{\partial Q_{e_g u}}\right)_0 \right| u \right\rangle - \left\langle v \left| \left(\frac{\partial V}{\partial Q_{e_g u}}\right)_0 \right| v \right\rangle + \left\langle \xi \left| \left(\frac{\partial V}{\partial Q_{e_g u}}\right)_0 \right| \xi \right\rangle + \left\langle \eta \left| \left(\frac{\partial V}{\partial Q_{e_g u}}\right)_0 \right| \eta \right\rangle \quad (17a)$$

$$F_{t_{2g}}{}^{5T_{2g}} - F_{t_{2g}}{}^{1A_{1g}} = -\left\langle {}^5T_{2g}\xi M_s \left| \left(\frac{\partial V}{\partial Q_{t_{2g\eta}}}\right)_0 \right| {}^5T_{2g}\zeta M_s \right\rangle = -\left\langle \xi \left| \left(\frac{\partial V}{\partial Q_{t_{2g\eta}}}\right)_0 \right| \zeta \right\rangle \quad (17b)$$

Because the ligands in $Co(NH_3)_6^{3+}$ are pure σ donors, the t_{2g} electrons are nonbonding; hence, the integrals over t_{2g} one-electron wave functions will be negligible. This eliminates the effects of the last two terms in eq 17a contributing to the e_g distortion and all the terms in eq 17b contributing to the t_{2g} distortion. Further, from the Wigner-Eckart theorem, $\langle u|(\partial V/\partial Q_{e_g u})_0|u\rangle = -\langle v|(\partial V/\partial Q_{e_g u})_0|v\rangle$, thus canceling any significant contribution from e_g electrons to the e_g distortion. Therefore we expect the Huang-Rhys parameter S_{e_g} to be close to zero in the $^5T_{2g}$ state. From crystal-field theory, the slope of a state on the Tanabe-Sugano diagram is proportional to the "restoring force" in the totally symmetric a_{1g} mode evaluated over the wave function (see ref 1).

$$\text{slope}\,(^5T_{2g}) = \left(\frac{\partial E(^5T_{2g})}{\partial Dq}\right) \propto \left\langle {}^5T_{2g} \left| \left(\frac{\partial V}{\partial Q_{a_{1g}}}\right)_0 \right| {}^5T_{2g} \right\rangle \quad (18)$$

and

$$\left\langle {}^5T_{2g} \left| \left(\frac{\partial V}{\partial Q_{a_{1g}}}\right)_0 \right| {}^5T_{2g} \right\rangle \propto S_{a_{1g}}{}^{1/2}(^5T_{2g}) \quad (19)$$

therefore

$$\left[\frac{\text{slope}(^5T_{2g})}{\text{slope}(^3T_{1g})}\right]^2 = \frac{S_{a_{1g}}(^5T_{2g})}{S_{a_{1g}}(^3T_{1g})} \quad (20)$$

Because the $^3T_{1g}$ and $^5T_{2g}$ result from one- and two-electron excitations, respectively, we find $S_{a_{1g}}(^5T_{2g}) = 4S_{a_{1g}}(^3T_{1g})$. Then from eq 4

$$\Delta Q \propto S^{1/2} \quad (21)$$

and we define a relative Huang-Rhys parameter between the $^5T_{2g}$ and $^3T_{1g}$ states

$$S_{a_{1g}}{}^{rel} = (S_{a_{1g}}{}^{1/2}(^5T_{2g}) - S_{a_{1g}}{}^{1/2}(^3T_{1g}))^2 \quad (22)$$

Using the value of $S_{a_{1g}}(^3T_{1g}) = 2.4$ found in section IVB we obtain $S_{a_{1g}}{}^{rel} = 2.4$. Since $S_{e_g}(^5T_{2g}) = 0$ we also have $S_{e_g}{}^{rel} = S_{e_g}(^3T_{1g}) = 3.7$. These parameters are then used in the evaluation of the necessary vibrational overlap integrals which are given as

$$\langle \alpha 000|\eta n_1 jk\rangle = \langle \alpha 000|\zeta n_1 jk\rangle = e^{-(S_{a_{1g}}{}^{rel}+S_{e_g}{}^{rel})/2} \times \frac{(S_{a_{1g}}{}^{rel})^{n_1/2}}{(n_1!)^{1/2}} \frac{(S_{e_g}{}^{rel})^{(j+k)/2}}{(j!k!)^{1/2}} (1/2)^j \left(\frac{3^{1/2}}{2}\right)^k$$

$$\langle \beta 000|\xi n_1 jk\rangle = \langle \beta 000|\zeta n_1 jk\rangle = e^{-(S_{a_{1g}}{}^{rel}+S_{e_g}{}^{rel})/2} \times \frac{(S_{a_{1g}}{}^{rel})^{n_1/2}}{(n_1!)^{1/2}} \frac{(S_{e_g}{}^{rel})^{(j+k)/2}}{(j!k!)^{1/2}} (1/2)^j \left(\frac{-3^{1/2}}{2}\right)^k \quad (23)$$

$$\langle \gamma 000|\xi n_1 jk\rangle = \langle \gamma 000|\zeta n_1 jk\rangle = e^{-(S_{a_{1g}}{}^{rel}+S_{e_g}{}^{rel})/2} \frac{(S_{a_{1g}}{}^{rel})^{n_1/2}}{(n_1!)^{1/2}} \frac{(S_{e_g}{}^{rel})^{(j+k)/2}}{(j!k!)^{1/2}} (-1)^j (0)^k$$

where n_1, j, k are the a_{1g}, $e_g u$, $e_g v$ quantum numbers, respectively, and $n_2 = j + k$ is the total number of quanta in the e_g mode.

Using these expressions, the vibronic $^3T_{1g}$–$^5T_{2g}$ Hamiltonian can be computer programmed and diagonalized for different values of the parameter Δ_{00}, and the calculated multiplet splitting of the $^3T_{1g}(0,0)$ level can then be compared to experiment. Because the dimension of this matrix goes as $9 + 15N_a(N_e + 1)(N_e + 2)/2$ (N_a and N_e are the maximum a_{1g} and e_g quantum numbers considered), it is impractical to diagonalize the resulting Hamiltonian for more than a few quanta in each mode. We therefore perform the calculation using a restricted set of levels and take the remaining levels of the $^5T_{2g}$ into account via a second-order interaction term which now includes the vibronic overlap integral. In the $^3T_{1g}$ effective Hamiltonian block, these second-order terms have the form for $\gamma' = \gamma''$

$$\langle {}^3T_{1g}\gamma' M_s' | H_{SO}{}^{(2)}(^5T_{2g}) | {}^3T_{1g}\gamma'' M_s'' \rangle = \langle {}^3T_{1g}\gamma' M_s' | H_{SO}{}^{(2)}(^5T_{2g}) | {}^3T_{1g}\gamma'' M_s'' \rangle G''(S_{a_{1g}}{}^{rel}, S_{e_g}{}^{rel}) \exp(-S_{a_1}{}^{rel} - S_{e_g}{}^{rel}) \quad (24)$$

for $\gamma' \neq \gamma''$

$$\langle {}^3T_{1g}\gamma' M_s' | H_{SO}{}^{(2)}(^5T_{2g}) | {}^3T_{1g}\gamma'' M_s'' \rangle = \langle {}^3T_{1g}\gamma' M_s' | H_{SO}{}^{(2)}(^5T_{2g}) | {}^3T_{1g}\gamma'' M_s'' \rangle G''\left(S_{a_{1g}}{}^{rel}, \frac{-S_{e_g}{}^{rel}}{2}\right) \exp(-S_{a_{1g}}{}^{rel} - S_{e_g}{}^{rel})$$

where

$$G''(x,y) = -\sum{}' \frac{x^{n_1} y^{n_2}}{n_1! n_2! (\Delta_{00} + n_1\hbar\omega_{a_{1g}} + n_2\hbar\omega_{e_g})}$$

(the primed sum excludes levels included in the restricted set) and $H_{SO}{}^{(2)}$ is a second-order Hamiltonian.

Using eq 16, 23, and 24 we can now set up the Hamiltonian matrix for the $^3T_{1g}$–$^5T_{2g}$ interaction and diagonalize it for different positive values of the parameter Δ_{00}. With $\Delta_{00} > 600$ cm^{-1}, the resultant calculated splittings (left-hand side of Figure 16) correspond to the "quenched limit" (see section IVC, Figure 15), with the Γ_1 and Γ_3 levels nearly coincident and separated from the lower Γ_4, Γ_5 levels (also nearly coincident) by approximately $\kappa + \rho$. This quenched limit pattern is significantly altered when a vibronic level of the $^5T_{2g}$ closely approaches the $^3T_{1g}(0,0)$ level. The magnitude of the effect

Table V. Experimental Huang-Rhys Parameters and Vibrational Energies for Photoactive Excited States[a]

	$S_{a_{1g}}$	S_{e_g}	$\hbar\omega_{a_{1g}}$	$\hbar\omega_{e_g}$	Δa	Δe
$^3T_{1g}$ – $Co(CN)_6^{3-}$	4.8	9.2	420[b]	420[b]	0.07	0.14
$^3T_{1g}$ – $Co(NH_3)_6^{3+}$	2.4	3.7	483	434	0.05	0.11
$^1T_{1g}$ – $Co(NH_3)_6^{3+}$	3.6	2.8	480	429	0.02	0.12
$^4T_{2g}$ – $Cr(NH_3)_6^{3+}$	2.7	2.3	403[b]	403[b]	0.02	0.12
$^5T_{2g}$ – $Co(NH_3)_6^{3+}$	9.6[c]	0[c]	435[c]		−0.12	0.12

[a] See Discussion. [b] Assumes Huang-Rhys approximation ($\hbar\omega_{a_{1g}} = \hbar\omega_{e_g}$). [c] Estimated (see text).

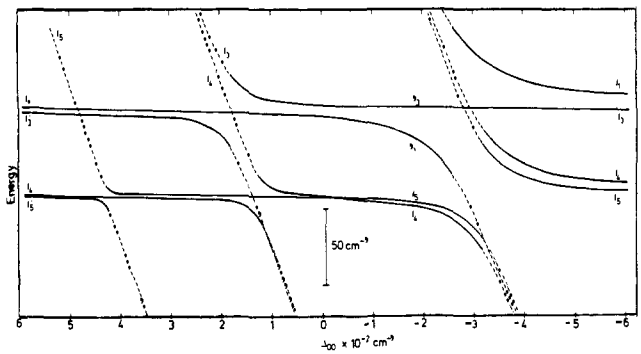

Figure 16. Effects of the $^5T_{2g}$ (0,0) position on the multiplet splittings of the $^3T_{1g}$ (0,0) level as determined from the vibronic manifold calculation. The parameter Δ_{00} is the energy difference between the $^5T_{2g}$ (0,0) and $^3T_{1g}$ (0,0) multiplet "centers of gravity". The dashed lines correspond to levels with ≥50% $^5T_{2g}$ electronic character. For this calculation the $^5T_{2g}$ [(0,0), (2,0), (0,3), (2,3)] restricted set was used.

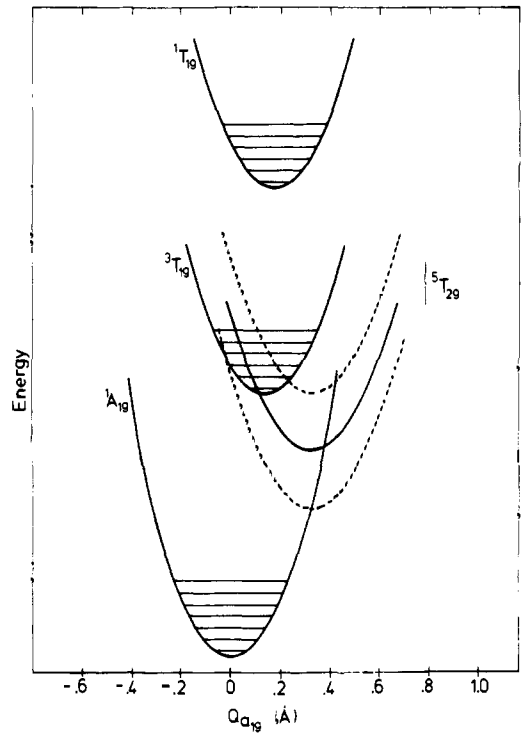

Figure 17. Potential-surface diagram for the $^1T_{1g}$, $^3T_{1g}$, $^5T_{2g}$, $^1A_{1g}$ electronic states in $Co(NH_3)_6^{3+}$ along the $\nu(a_{1g})$ vibrational coordinate. The two dashed $^5T_{2g}$ curves represent the upper and lower limits on the $^5T_{2g}$ surface. The solid $^5T_{2g}$ curve corresponds to the surface obtained having the $^5T_{2g}$ (2,3) level (largest overlap factor) closest in energy to the $^3T_{1g}$ (0,0) level.

of each vibronic level of the $^5T_{2g}$ upon the triplet multiplet splittings will depend upon two factors: the size of the vibrational overlap integral and the energy difference between the two levels. Using the values of $S_{a_{1g}}^{rel}$ and $S_{e_g}^{rel}$ already determined, the largest overlap factor occurs for the level with $n_1 = 2$ (a_{1g}) and $n_2 = 3$ (e_g). With Δ_{00} positive, the level closest to the $^3T_{1g}(0,0)$ state is the $^5T_{2g}$ level with $n_1 = n_2 = 0$, which is the lowest level of the $^5T_{2g}$ state. Therefore, as Δ_{00} is decreased, the $^5T_{2g}(0,0)$ level is the first state which may cause significant changes in the quenched limit pattern of the $^3T_{1g}$ multiplet. In Figure 16 we show the energy level diagram (as a function of Δ_{00}) for the $^3T_{1g}(0,0)$ and $^5T_{2g}$ states in the region where the $^5T_{2g}(0,0)$ level is strongly interacting. For this calculation $^5T_{2g}[(0,0), (2,0), (0,3), (2,3)]$ was chosen as the restricted set. The dashed curves correspond to levels having electronic $^5T_{2g}$ character ≥50%, and thus transitions to these states will be relatively weak owing to the very forbidden nature of the $^5T_{2g}$. Experiment requires either a $^3T_{1g}$ (solid curves) Γ_3 or Γ_5 component approximately 70 cm^{-1} below a Γ_4 component, which does not occur in the diagram. This is primarily due to the relatively small value of the vibrational overlap factor for the $^5T_{2g}(0,0)$ level, and prevents the $^3T_{1g}$ levels from significantly deviating in energy before their electronic character becomes mostly $^5T_{2g}$. For higher interacting vibronic levels ($\Delta_{00} < 0$) in the $^5T_{2g}$ (up to $n_1 = 2$, $n_2 = 3$), the overlap factors are larger and splitting patterns consistent with the observed pattern can be obtained. However, owing to the large number of possible interacting $^5T_{2g}$ vibronic levels which give reasonable splitting patterns, and the approximate nature of the calculation (estimated parameters, etc), it is not possible to reliably determine the exact position of the $^5T_{2g}$ potential surface. Instead we use Figure 16 to place the upper limit on the $^5T_{2g}$ surface, such that Δ_{00} must be negative ($^5T_{2g}(0,0) < {}^3T_{1g}(0,0)$) in order to find agreement with experiment. We also use the results of this calculation to infer a lower limit on the $^5T_{2g}$ surface by noting the approximately symmetrical manner in which the vibronic overlap factors vary in magnitude as a function of n_1 and n_2. These factors increase up to the $n_1 = 2$, $n_2 = 3$, level (which is approximately 2300 cm^{-1} above the $n_1 = n_2 = 0$ level), at which point they begin to decrease. Levels about 4600 cm^{-1} above $^5T_{2g}(0,0)$ (2300 cm^{-1} above $n_1 = 2$, $n_2 = 3$) will have overlap factors with roughly the same magnitude as the $^5T_{2g}(0,0)$ and thus will also be ineffective in causing large enough variations in the $^3T_{1g}(0,0)$ multiplet orderings to be in agreement with experiment. We therefore determine $0 > \Delta_{00} > -4600$ cm^{-1} as the possible energy range of the $^5T_{2g}$ state which is consistent with the observed $^3T_{1g}(0,0)$ multiplet splittings. We are thus able to determine the approximate position of the $^5T_{2g}$ potential surface via its interaction with the directly observable $^3T_{1g}$ electronic origins and obtain the potential-surface diagram for the lowest excited states of $Co(NH_3)_6^{3+}$.

In Figure 17 we present the approximate potential surface diagram for the $^1A_{1g}$, $^1T_{1g}$, $^3T_{1g}$, and $^5T_{2g}$ states along the totally symmetric a_{1g} vibrational coordinate. Previously we have assumed equal force constants in the $^3T_{1g}$ and $^5T_{2g}$ states in order to obtain estimates of the parameters needed in the calculations; in the figure we have allowed for a 10% reduction in the $^5T_{2g}$ vibrational frequency to account for bond-strength reduction in this $2e^-$ excited state. The approximate upper and lower limits on the position of the $^5T_{2g}$ potential surface are indicated by the dashed curves, with the solid curve representing the surface having the (2,3) level strongly interacting with the lowest vibronic level of the $^3T_{1g}$. We next discuss the

implications of this diagram on the photophysical and photochemical properties of $Co(NH_3)_6^{3+}$ and related complexes.

VI. Discussion

From the values of S and $\hbar\omega$ collected in Table V for each excited state and the use of eq 4, we can obtain distortions in the a_{1g} and e_g normal modes, which can further be written in terms of metal-ligand distortions (see eq 21, ref 1). The excited-state geometries, which have been experimentally obtained in the cases of the $^1T_{1g}$ and $^3T_{1g}$ states and predicted from ligand field theory for the $^5T_{2g}$ state, are sketched in Figure 18 with values of the parameters Δa (axial bond length change) and Δe (equatorial bond length change) given in Table V. Analogous results for the $^4T_{2g}$ state of $Cr(NH_3)_6^{3+}$ and the $^3T_{1g}$ of $Co(CN)_6^{3-}$ are also included in Table V. For the $Co(CN)_6^{3-}$, we have separated the a_{1g} and e_g contributions to the effective S_{eff} (≈ 14)[5a] $= S_{a_{1g}} + S_{e_g}$ by estimating $S_{a_{1g}}$ for $Co(CN)_6^{3-}$ from the value of $S_{a_{1g}}$ for $Co(NH_3)_6^{3+}$. The relationship between these two quantities can be obtained from crystal field theory and is given as

$$\frac{S_{a_{1g}}{}^{c}}{S_{a_{1g}}{}^{a}} = \left(\frac{Dq^c}{Dq^a}\right)^2\left(\frac{R^a}{R^c}\right)^2\left(\frac{k^a\hbar\omega^a}{k^c\hbar\omega^c}\right) \qquad (25)$$

where the a and c refer to ammine and cyanide, respectively. Since we have already determined $S_{a_{1g}}$ for $Co(NH_3)_6^{3+}$, by inserting the appropriate parameters in eq 25, we obtain an estimate of $S_{a_{1g}} = 4.8$ and then $S_{e_g} = 9.2$ in $Co(CN)_6^{3-}$. Thus we see (Figure 18, Table V) that, while the $^3T_{1g}$ of $Co(CN)_6^{3-}$ is somewhat distorted, the $^3T_{1g}$ of $Co(NH)_6^{3+}$ and the $^4T_{2g}$ of $Cr(NH_3)_6^{3+}$ also have large distortions and a D_{4h} equatorially expanded geometry. Thus it is unlikely that the large differences in photochemical quantum yield relate to these differences in excited-state distortions. It is more reasonable to associate these distortions with the mechanism of photolabilization of the complex. In this regard, our vibrational analysis of the absorption and emission band shapes of the transitions to the photoactive $^3T_{1g}$ and $^4T_{2g}$ states demonstrates that these states are bound. Thus the photochemical mechanism is not the result of direct excitation into a dissociative state. However, large a_{1g} and e_g distortions in the excited state may result in a sizable Franck-Condon overlap with the continuum levels of the ground state, resulting in a stereospecific (in derivative C_{4v} and D_{4h} complexes) photochemical reaction if the e_g contribution is large.

It is further seen from Figure 17 that, for any position within the determined allowable range, the $^5T_{2g}$ adiabatic surface crosses the $^3T_{1g}$ surface near its minimum. Because the $^3T_{1g}$ and $^5T_{2g}$ states interact in first order via spin-orbit coupling, the effect of this will be an efficient radiationless pathway (with small thermal activation energy) from the $^3T_{1g}$ state into the $^5T_{2g}$ state. The rate of radiationless deactivation of the $^3T_{1g}$ state will compete with other excited-state processes, such as radiative deactivation (emission) and photochemical reaction. This observation is pertinent with respect to a comparison of these processes in $Co(NH_3)_6^{3+}$ and $Co(CN)_6^{3-}$. In the cyanide complex, Dq is large and the $^5T_{2g}$ state will be shifted to higher energy with respect to the $^3T_{1g}$ state, eliminating the $^3T_{1g} \rightsquigarrow {}^5T_{2g}$ pathway. The photoaquation quantum yield for $Co(CN)_6^{3-}$ is 0.31[4a] as compared to 3.1×10^{-4} [4a] for $Co(NH_3)_6^{3+}$. Further, $K_3Co(CN)_6$ readily emits ($\phi = 0.05$ at 77 K),[18] whereas no emission has been reported for $Co(NH_3)_6^{3+}$, although emission for this complex is expected to be in an experimentally difficult region (predicted $h\nu_{max} = 7250\ cm^{-1}$). Accepting that efficient transfer of excitation into the $^5T_{2g}$ takes place, the quantum yield for photoaquation in the $^5T_{2g}$ must also be small. Just the opposite might have been expected in view of its spin multiplicity (long lifetime), doubly excited electron configuration, and associated large a_{1g} distortion (Figure 17). However, the potential minimum of the $^5T_{2g}$ intersects the $^1A_{1g}$ potential surface. In this case, higher order spin-orbit plus configurational mixing must be invoked for $^1A_{1g}$–$^5T_{2g}$ interaction to occur, leading to further radiationless deactivation into the ground state. If this interaction is significant, then the deexcitation pathway is complete and all excited-state photochemical processes ($^3T_{1g}$ or $^5T_{2g}$) will be strongly diminished.

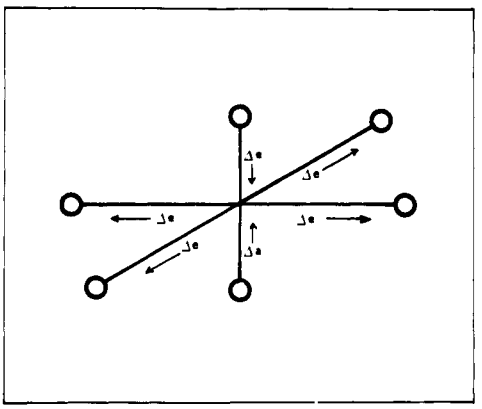

Figure 18. Experimental geometries of the excited states summarized in Table V. The parameters Δa and Δe are the magnitudes of the bond-length changes in the directions indicated.

Acknowledgment. This work was supported by The Cabot Solar Energy Fund. We thank Professors Mark Wrighton and Bob Silbey for useful discussions.

References and Notes

(1) R. B. Wilson and E. I. Solomon, *Inorg. Chem.*, **17**, 1729 (1978). In this reference, the notation and phases used are those of Griffith. For the present study we use notation and phases of Tanabe, Sugano, and Kamimura, ref 9.
(2) R. A. Pribush, C. K. Poon, C. M. Bruce, and A. W. Adamson, *J. Am. Chem. Soc.*, **96**, 3027 (1974).
(3) C. H. Langford and C. P. J. Vuik, *J. Am. Chem. Soc.*, **98**, 5409 (1976).
(4) (a) E. Zinato in "Concepts of Inorganic Photochemistry", A. W. Adamson and P. D. Fleischauer, Eds., Wiley-Interscience, New York, 1975, Chapter 4, p 143, and references cited therein; (b) P. D. Fleischauer, A. W. Adamson, and G. Sartori, *Prog. Inorg. Chem.*, **17**, 1 (1972); (c) M. S. Wrighton, *Top. Curr. Chem.*, **65** (1976); (d) V. Balzani and V. Carassiti, "Photochemistry of Coordination Compounds", Academic Press, New York, 1975, p 195.
(5) (a) V. M. Miskowski, H. B. Gray, R. B. Wilson, and E. I. Solomon, *Inorg. Chem.*, **18**, 1410 (1979); (b) K. W. Hipps and G. A. Crosby, *ibid.*, **13**, 1543 (1974).
(6) J. Bjerrum and J. P. McReynolds, *Inorg. Synth.*, **2**, 216 (1946).
(7) H. Siebert and H. H. Eysel, *J. Mol. Struct.*, **4**, 29 (1969).
(8) K. Okumura, *J. Phys. Soc. Jpn.*, **17**, 1341 (1962).
(9) S. Sugano, Y. Tanabe, and H. Kamimura, "Multiplets of Transition-Metal Ions in Crystals", Academic Press, New York, 1970.
(10) D. B. Fitchen in "Physics of Color Centers", W. B. Fowler, Ed., Academic Press, New York, 1968, p 293.
(11) Y. Tanabe and S. Sugano, *J. Phys. Soc. Jpn.*, **9**, 753 (1954).
(12) M. D. Sturge, *Phys. Rev. B*, **1**, 1005 (1970). Here the sign of the term in λ is changed to correspond to a T_1 state.
(13) K. A. Schroeder, *J. Chem. Phys.*, **37**, 2553 (1962).
(14) T. M. Dunn, *Trans. Faraday Soc.*, **57**, 1441 (1961).
(15) Here we have neglected the term corresponding to the t_{2g} normal mode as there is no experimental evidence for such a distortion in this molecule. This is what might be expected for a complex of pure σ donor ligands (see section VB).
(16) F. S. Ham, *Phys. Rev. A*, **138**, 1727 (1965).
(17) H. U. Güdel and T. R. Snellgrove, *Inorg. Chem.*, **17**, 1617 (1978).
(18) (a) M. Mingardi and G. B. Porter, *J. Chem. Phys.*, **44**, 4354 (1966); (b) K. W. Hipps and G. A. Crosby, *Inorg. Chem.*, **13**, 1543 (1974); (c) A. Wolpl and D. Oelkrug, *Ber. Bunsenges. Phys. Chem.*, **79**, 394 (1975).